

Two-dimensional square-Au_2S monolayer: A promising thermoelectric material with ultralow lattice thermal conductivity and high power factor

Wei Zhang(张伟), Xiao-Qiang Zhang(张晓强), Lei Liu(刘蕾), Zhao-Qi Wang(王朝棋), and Zhi-Guo Li(李治国)
Citation: Chin. Phys. B, 2021, 30 (**7**): 077405. DOI: 10.1088/1674-1056/abe115
Journal homepage: http://cpb.iphy.ac.cn; http://iopscience.iop.org/cpb

What follows is a list of articles you may be interested in

Superconductivity in an intermetallic oxide $Hf_3Pt_4Ge_2O$

Chengchao Xu(徐程超), Hong Wang(王鸿), Huanfang Tian(田焕芳), Youguo Shi(石友国), Zi-An Li(李子安), Ruijuan Xiao(肖睿娟), Honglong Shi(施洪龙), Huaixin Yang(杨槐馨), and Jianqi Li(李建奇)
Chin. Phys. B, 2021, 30 (**7**): 077403. DOI: 10.1088/1674-1056/abfb53

First-principles calculation of the structural,electronic,and magnetic properties of cubic perovskite Rb*X*F_3(*X*=Mn,V,Co,Fe)

Muhammad Raza ur rehman Hashmi, Muhammad Zafar, M Shakil, Atif Sattar, Shabbir Ahmed, S A Ahmad
Chin. Phys. B, 2016, 25 (**11**): 117401. DOI: 10.1088/1674-1056/25/11/117401

Superconductivity of bilayer phosphorene under interlayer compression

Gui-Qin Huang(黄桂芹) and Zhong-Wen Xing(邢钟文)
Chin. Phys. B, 2016, 25 (**2**): 027402. DOI: 10.1088/1674-1056/25/2/027402

First-principles study of FeSe epitaxial films on $SrTiO_3$

Liu Kai, Gao Miao, Lu Zhong-Yi, Xiang Tao
Chin. Phys. B, 2015, 24 (**11**): 117402. DOI: 10.1088/1674-1056/24/11/117402

First-principles study of orbital ordering in cubic fluoride $KCrF_3$

Ming Xing, Xiong Liang-Bin, Xu Huo-Xi, Du Fei, Wang Chun-Zhong, Chen Gang
Chin. Phys. B, 2014, 23 (**3**): 037401. DOI: 10.1088/1674-1056/23/3/037401

Two-dimensional square-Au_2S monolayer: A promising thermoelectric material with ultralow lattice thermal conductivity and high power factor*

Wei Zhang(张伟)[1], Xiao-Qiang Zhang (张晓强)[1], Lei Liu(刘蕾)[1,†], Zhao-Qi Wang(王朝棋)[2,‡], and Zhi-Guo Li(李治国)[3,§]

[1] School of Science, Southwest University of Science and Technology, Mianyang 621010, China
[2] Institute of Atomic and Molecular Physics, Sichuan University, Chengdu 610065, China
[3] Laboratory for Shock Wave and Detonation Physics, Institute of Fluid Physics, Mianyang 610064, China

(Received 11 November 2020; revised manuscript received 14 January 2021; accepted manuscript online 29 January 2021)

The search for new two-dimensional (2D) harvesting materials that directly convert (waste) heat into electricity has received increasing attention. In this work, thermoelectric (TE) properties of monolayer square-Au_2S are accurately predicted using a parameter-free *ab initio* Boltzmann transport formalism with fully considering the spin–orbit coupling (SOC), electron–phonon interactions (EPIs), and phonon–phonon scattering. It is found that the square-Au_2S monolayer is a promising room-temperature TE material with an n-type (p-type) figure of merit $ZT = 2.2$ (1.5) and an unexpected high n-type $ZT = 3.8$ can be obtained at 600 K. The excellent TE performance of monolayer square-Au_2S can be attributed to the ultralow lattice thermal conductivity originating from the strong anharmonic phonon scattering and high power factor due to the highly dispersive band edges around the Fermi level. Additionally, our analyses demonstrate that the explicit treatments of EPIs and SOC are highly important in predicting the TE properties of monolayer square-Au_2S. The present findings will stimulate further the experimental fabrication of monolayer square-Au_2S-based TE materials and offer an in-depth insight into the effect of SOC and EPIs on TE transport properties.

Keywords: first-principles calculations, electron–phonon interactions, lattice thermal conductivity, thermoelectric properties

PACS: 74.78.–w, 74.25.fg, 63.22.–m **DOI:** 10.1088/1674-1056/abe115

1. Introduction

Owing to increasingly severe environmental pollution and the depletion of fossil fuels, the search for alternative clean and renewable energy sources is urgent. Thermoelectric (TE) materials can spontaneously convert waste heat into electric energy, so they have great potential applications in alleviating the dilemmas of energy sources.[1–5] The performance of a TE material can be described by the dimensionless figure of merit $ZT = S^2\sigma T/(\kappa_l + \kappa_e)$, where S, σ, T, κ_l, and κ_e denote the Seebeck coefficient, electrical conductivity, absolute temperature, lattice thermal conductivity, and electronic thermal conductivity, respectively. High-performance TE materials usually require both high power factor ($PF = S^2\sigma$) and low total thermal conductivity κ ($\kappa = \kappa_l + \kappa_e$). Consequently, some techniques such as chemical doping, band structure engineering, strain engineering, nano-structuring, and low-dimensional structure were adopted to enhance PF or reduce κ.[6–10] Low-dimensional materials could exhibit significantly higher ZT values than their bulk counterparts[11,12] due to the decreased κ on account of the phonon boundary scattering and the improved PF caused by the quantum confinement effect.

Recently, the two-dimensional (2D) transition-metal chalcogenides M_2X (M = metal and X = S, Se, Te) have attracted considerable attention due to their nontrivial properties.[13–20] Monolayer δ-Cu_2S had an ultralow κ_l of 0.10 W/mK at 800 K, leading to a high ZT of 1.33.[14] The ZT of the metal-shrouded Tl_2O monolayer exceeded 3 when $T > 700$ K.[20] Monolayer Ag_2S was also recommended as a promising 2D TE material.[17] Recently, Chen *et al.*[18] and Wu *et al.*[19] proposed a new nonmetal-shrouded M_2X: monolayer square-Au_2S. Its cohesive energy 3.4 eV was comparable to that of monolayer Ge (3.26 eV) and Si (3.98 eV),[21] indicating the possibility to synthesize it experimentally. Cheng *et al.*[18] calculated the lattice thermal conductivity of this monolayer and found that it has an unusually low κ_l, but the physical origins behind such a low κ_l are unexplored. They also suggested that monolayer square-Au_2S has ultrahigh carrier mobilities. However, the carrier mobilities of monolayer square-Au_2S calculated by them were very different (their dif-

*Project supported by the Doctoral Research Fund of Southwest University of Science and Technology (Grant No. 21zx7113) and the National Natural Science Foundation of China (Grant Nos. 11804284 and 11802280).

†Corresponding author. E-mail: lei_liuchn@163.com
‡Corresponding author. E-mail: zhqwangsc@foxmail.com
§Corresponding author. E-mail: zhiguo_li@foxmail.com

© 2021 Chinese Physical Society and IOP Publishing Ltd

ference was more than 160%), though the same deformation potential theory was used.[22,23] This is due to the fact that the simplified phenomenological model they used contains some tunable parameters, and thus generally lacks sufficient predictive power.[24,25] Therefore, it is necessary to perform the parameter-free first-principles calculations for the electronic transport properties of monolayer square-Au_2S to obtain reliable results. Furthermore, we notice that previous work focused only on carrier mobilities, the full thermoelectric transport parameters like S, σ, κ_e, and PF for deriving the figure of merit ZT are still lacking.

In general, the electronic transport properties are computed in terms of the Boltzmann transport equation (BTE) within the constant relaxation time approximation (CRTA).[26–28] Actually, the carrier relaxation time relies on carrier mode, carrier concentration, and temperature.[25] Recently, the electronic transport properties could be accurately predicted by solving the parameter-free BTE under self-energy relaxation time approximation (SERTA) with the scattering limited by the electron-phonon interactions. In addition, as is well known, the spin–orbit coupling (SOC) effect may have a significant influence on the electronic band structure of materials and, further, on electronic transport properties.[29,30] Motivated by the above considerations, in this work, we aim to explore the origin of the low κ_l of monolayer square-Au_2S and investigate the full TE transport properties together with the ZT from first-principles calculations and parameter-free BTE. We find that this monolayer possesses a large n-type (p-type) $ZT = 2.2$ (1.5) at 300 K and $ZT = 3.8$ (2.5) at 600 K, indicating that it can become a highly promising room- and high-temperature TE material. Furthermore, the effects of EPIs and SOC on TE properties of the monolayer are also discussed.

2. Computational method

All first-principles calculations based on density functional theory (DFT) were performed by using the Quantum ESPRESSO package.[31] with Perdew–Burke–Ernzerhof (PBE) exchange–correlation functional.[32] The norm-conserving pseudopotential[33] was used to describe the core-valence interaction with a plane wave kinetic energy cutoff of 80 Ry (1 Ry = 13.6056923(12) eV). The convergence threshold of 1×10^{-8} a.u. (a.u. is short for atomic unit) for total energy and 1×10^{-5} a.u. for forces were used. The DFT-D3 method[34] was used to take into account the long-range van der Waals interaction. The electronic band structures were calculated by the six versions of Heyd–Scuseria–Ernzerh hybrid functional (HSE06). The spin–orbit coupling (SOC) interaction was considered in the calculations of electronic band structure and phonon dispersion. In *ab initio* molecular dynamics (AIMD) simulations, a $3 \times 3 \times 1$ supercell was used as an initial structure. The timestep and total simulation time were set to be 1 fs and 10 ps, respectively. The lattice thermal conductivity can be obtained by the self-consistent solution of the BTE, as implemented in the ShengBTE package.[35] The 2nd-order interatomic force constants (IFCs) with a $5 \times 5 \times 1$ $\boldsymbol{q}$-mesh were calculated by the density functional perturbation theory. A $3 \times 3 \times 1$ supercell and $5 \times 5 \times 1$ $\boldsymbol{k}$-mesh were used to calculate the 3rd-order anharmonic IFCs, and the interactions up to the eighth nearest-neighbors were included. In the BTE calculations, a dense Γ-centered $50 \times 50 \times 1$ $\boldsymbol{q}$-mesh was adopted to obtain converged results. The vacuum length L is set to be 20 Å, which avoids the interactions between layers. For properties requiring volume normalization, an effective thickness of 6.19 Å was used, which includes the bucking distance h of the monolayer plus twice the van der Waals radius of a sulfur atom.[18,25,27,36,38]

The EPI matrix elements were computed by using an initial coarse $15 \times 15 \times 1$ $\boldsymbol{k}$-mesh with a $5 \times 5 \times 1$ $\boldsymbol{q}$-mesh, and then interpolated to a dense $150 \times 150 \times 1$ $\boldsymbol{k}$-mesh with a $50 \times 50 \times 1$ $\boldsymbol{q}$-mesh using the maximally localized Wannier functions, as implemented in the EPW package.[39,40] These settings are enough to ensure convergence. The energy-resolved carrier relaxation time of the electronic state with band index n and wave vector $\boldsymbol{k}$ can be estimated from the imaginary part of the electron self-energy $\mathrm{Im}(\Sigma)$ as follows:

$$\begin{aligned}\frac{1}{\tau_{n\boldsymbol{k}}(E)} &= \frac{2\mathrm{Im}(\Sigma)}{\hbar} \\ &= \frac{2\pi}{\hbar}\sum_{m\nu}\int \frac{\mathrm{d}\boldsymbol{q}}{\Omega_{\mathrm{BZ}}} |g_{mn\nu}(\boldsymbol{k},\boldsymbol{q})|^2 \\ &\quad \times \left[\left(1 - f^0_{m\boldsymbol{k}+\boldsymbol{q}} + n_{\boldsymbol{q}\nu}\right) \delta\left(\varepsilon_{n\boldsymbol{k}} - \varepsilon_{m\boldsymbol{k}+\boldsymbol{q}} - \hbar\omega_{\boldsymbol{q}\nu}\right) \right. \\ &\quad \left. + \left(f^0_{m\boldsymbol{k}+\boldsymbol{q}} + n_{\boldsymbol{q}\nu}\right) \delta\left(\varepsilon_{n\boldsymbol{k}} - \varepsilon_{m\boldsymbol{k}+\boldsymbol{q}} + \hbar\omega_{\boldsymbol{q}\nu}\right) \right], \end{aligned} \tag{1}$$

where Ω_{BZ} is the volume of the first Brillouin zone, matrix elements $g_{mn\nu}(\boldsymbol{k},\boldsymbol{q})$ are the probability amplitude for scattering from an initial electronic state $|n\boldsymbol{k}\rangle$ into a final state $|m\boldsymbol{k}+\boldsymbol{q}\rangle$ via a phonon $\boldsymbol{q}\nu$, $f_{n\boldsymbol{k}}$ is the Fermi–Dirac distribution function, $n_{\boldsymbol{q}\nu}$ is the Bose–Einstein distribution function, $\varepsilon_{n\boldsymbol{k}}$ is the electron eigenvalue for the state $|n\boldsymbol{k}\rangle$, $\omega_{\boldsymbol{q}\nu}$ is the phonon frequency of wave vector $\boldsymbol{q}$, and branch index ν. Then, based on the $\tau_{n\boldsymbol{k}}(E)$ and band structure from HSE06 with SOC, the electronic transport coefficients, including S, σ, and κ_e, can be obtained as follows:

$$S = -\frac{1}{eT}\frac{\sum_{n\boldsymbol{k}}\left(\varepsilon_{n\boldsymbol{k}} - \varepsilon_{\mathrm{F}}\right)\left(v_{n\boldsymbol{k}}\right)^2 \tau_{n\boldsymbol{k}}(E)\frac{\partial f_{n\boldsymbol{k}}}{\partial \varepsilon_{n\boldsymbol{k}}}}{\sum_{n\boldsymbol{k}}\left(v_{n\boldsymbol{k}}\right)^2 \tau_{n\boldsymbol{k}}(E)\frac{\partial f_{n\boldsymbol{k}}}{\partial \varepsilon_{n\boldsymbol{k}}}}, \tag{2}$$

$$\sigma = -\frac{e^2}{N_k \Omega}\sum_{n\boldsymbol{k}}\left(v_{n\boldsymbol{k}}\right)^2 \tau_{n\boldsymbol{k}}(E)\frac{\partial f_{n\boldsymbol{k}}}{\partial \varepsilon_{n\boldsymbol{k}}}, \tag{3}$$

$$\kappa_e = -\frac{1}{N_k \Omega T}\sum_{n\boldsymbol{k}}\left(\varepsilon_{n\boldsymbol{k}} - \varepsilon_{\mathrm{F}}\right)^2\left(v_{n\boldsymbol{k}}\right)^2 \tau_{n\boldsymbol{k}}(E)\frac{\partial f_{n\boldsymbol{k}}}{\partial \varepsilon_{n\boldsymbol{k}}} - TS^2\sigma, \tag{4}$$

where e, N_k, Ω, ε_F, and $v_{n\boldsymbol{k}}$ represent the electron charge, total number of $\boldsymbol{k}$-points, volume of the unit cell, Fermi energy, and electron group velocity, respectively. The electronic transport coefficients were solved by using the BoltzTraP2 package.[27] Hereinafter, we refer to this computational scheme as SOC+SERTA. To elucidate the influence of EPIs on the electronic transport coefficients, the CRTA and SERTA calculations without the SOC were carried out (referred to as NoSOC + CRTA and NoSOC + SERTA hereinafter). The role of the SOC effect is checked by comparing the SOC + SERTA calculations with the NoSOC + SERTA calculations. In the CRTA calculations, the carrier relaxation time τ was calculated from the equation: $\tau = \mu m^*/e$, where carrier mobility μ and effective mass m^* were cited from Ref. [18].

3. Results and discussion

3.1. Structure of monolayer square-Au_2S

Monolayer square-Au_2S has a tetragonal structure with a space group symmetry of $P4/nmm$. There are four Au atoms and two S atoms in a unit cell, and the four Au atoms are in a plane. The layer of Au atoms is sandwiched between two layers of S atoms, and each S atom is tetracoordinated with Au atoms as shown in Figs. 1(a) and 1(b). The fully optimized lattice parameter and the bucking distance h of monolayer square-Au_2S are 5.74 Å and 2.59 Å, respectively. These structural parameters accord well with previous calculations.[19] The phonon dispersion and AIMD simulations indicate that the monolayer square-Au_2S possesses good dynamical and thermal stability (see the supplementary material, Fig. S1). Figure 1(c) displays the electron localization functions, from which we can see that the electrons are mostly localized near S atoms, implying the ionic nature of the Au–S bond. In general, weak interatomic bonding is an indicator of low κ_l.[7]

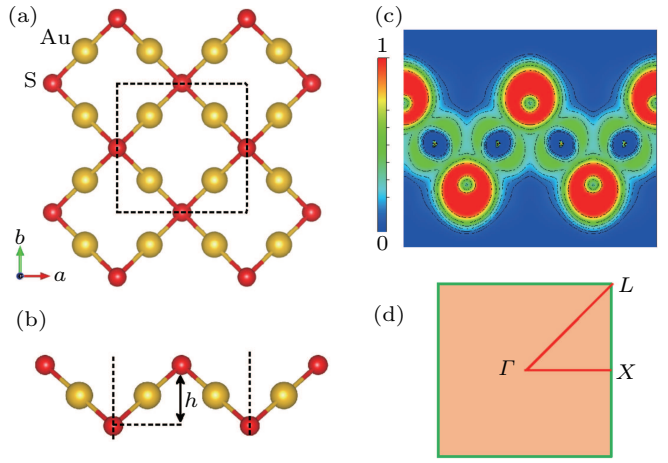


Fig. 1. (a) Top view and (b) side view of the atomic structure of monolayer square-Au_2S, (c) electron localization functions, and (d) high-symmetry k-points in the first Brillouin zone.

3.2. Lattice thermal conductivity

The calculated κ_l *versus* temperature is displayed in Fig. 2(a). As expected, monolayer square-Au_2S has an ultralow κ_l of 0.72 W/mK at room temperature, which is smaller than other 2D nanosheets have, like SnSe,[41] Bi_2Te_3,[42] MoS_2,[43] BP,[44] PdS_2,[3] and comparable to those of the recently reported monolayers Tl_2O[13] and Bi_2O_2Se.[6] The ultralow κ_l of monolayer square-Au_2S is beneficial to the high TE performance. It can also be seen from Fig. 2(a) that the κ_l of monolayer square-Au_2S decreases with temperature increasing, reaching 0.48 W/mK at 600 K. This is mainly due to the inherent enhancement of the phonon–phonon scattering with temperature increasing. It is noted that our calculated κ_l of monolayer square-Au_2S is lower than that in Ref. [18], which is because the van der Waals interaction exerts influence on group velocity and the phonon relaxation time is included in the present work. The calculated contributions from different phonon branches to κ_l in Fig. 2(b) reveal that low-frequency acoustic branches contribute to the majority of the κ_l. In contrast, the contribution from high-frequency optical branches is quite small.

According to phonon Boltzmann theory, κ_l is proportional to the phonon lifetime and the square of the group velocity.[28] Thus, to understand the origin of such an ultralow κ_l, the phonon group velocities and relaxation time *versus* frequency are shown in Figs. 2(c) and 2(d), respectively. The group velocities and phonon lifetime from the acoustic branches are higher than those from the optical branches, which helps explain why the contribution from acoustic branches accounts for the majority of κ_l. The maximum phonon group velocity of all phonon modes for monolayer square-Au_2S is quite small (within 3 km/s), resulting in the low κ_l. On the other hand, the phonon lifetimes for the acoustic modes are low enough (1 ps–100 ps), which implies the strong phonon scattering. The anharmonic phonon scattering can be characterized by two parameters: the Grüneisen parameter γ and the size of the three-phonon scattering phase space W. The mode Grüneisen parameter and weighted phase space of three-phonon scattering of the acoustic branches are both large (see Fig. S2 in Supplementary Material), leading to low phonon lifetime and, hence, low κ_l.

It is worth noting that EPIs may have an important effect on phonon thermal conductivity.[45,46] However, the present calculations elucidate that the phonon relaxation time arising from the intrinsic phonon–phonon scattering is at least two orders of magnitude smaller than that from electron–phonon scattering (see Fig. S3 in supplementary material). Therefore, according to Matthiessen's rule,[28] the κ_l of monolayer square-Au_2S due to EPIs can be safely ignored.

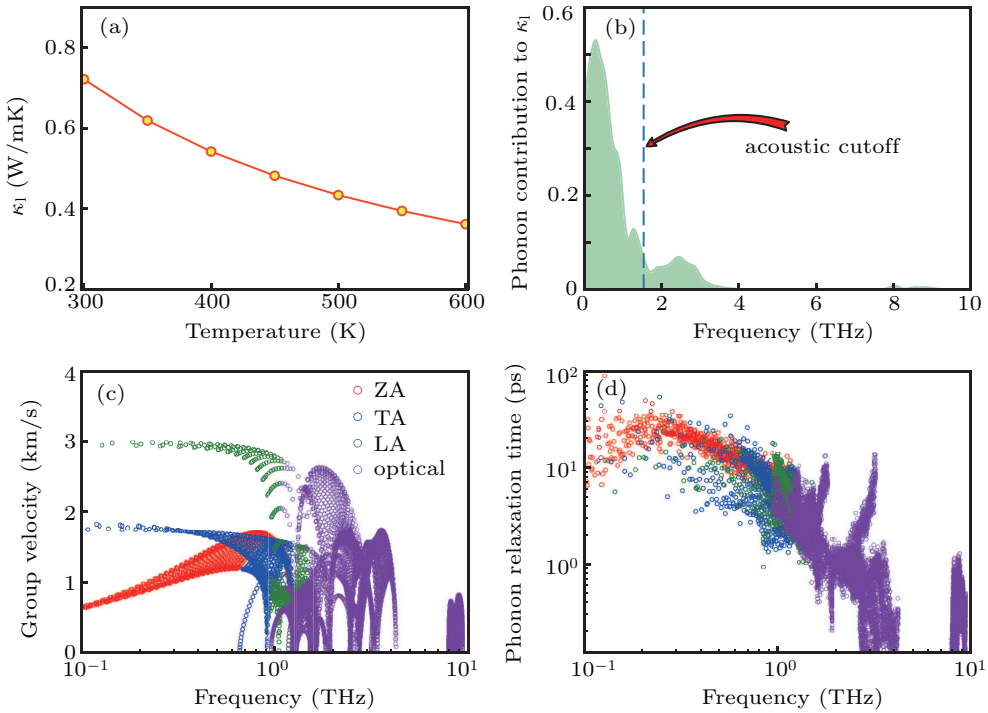


Fig. 2. (a) Lattice thermal conductivity κ_l *versus* temperature, (b) contribution of phonons at different frequencies to κ_l, and (c) phonon group velocity, and (d) phonon relaxation time *versus* frequency at 300 K for monolayer square-Au_2S.

3.3. Electronic transport and TE properties

Monolayer square-Au_2S with low κ_l will be a highly useful TE material if its S and σ are high enough. The electronic transport properties depend mainly on the band structure and carrier relaxation time. We use the hybrid functional HSE06 to overcome the underestimation of bandgap by PBE. As shown in Fig. 3(a), monolayer square-Au_2S is a semiconductor with a direct bandgap of 0.8 (1.2) eV with (without) SOC, which is slightly smaller than that reported in Ref. [19]. The projected density of states shown in Fig. 3(b) indicate that both Au atoms and S atoms contribute to states near the Fermi level, implying that there is a strong hybridization between orbitals of Au and S atoms. Further analyses of the orbital-resolved density of states (see Fig. S4) indicate that the states near the valence band maximum (VBM) are contributed mainly by the hybridization of atomic orbitals of Au atoms and atomic orbitals of S atom. The states around the conduction band minimum (CBM), however, stem mainly from the atomic orbitals of the Au atom. Consequently, the valence band and conduction band may have different dispersion characteristics as shown in Fig. 3(a). There exists strong dispersion near the CBM, while the bands around the VBM are relatively flat. Upon the introduction of the SOC effect, the band edges near the VBM become more dispersive, while the band shape around the CBM is hardly affected. Therefore, after including SOC, the band edges around the Fermi level are highly dispersive, leading to small effective mass ($m^* = 0.06m_e$ for electron and $m^* = 0.10m_e$ for hole[19]). According to the deformation potential theory, the carrier mobility μ is inversely proportional to effective mass m^*. And the electronic conductivity σ can be calculated from the equation: $\sigma = \mu ne$, where n is carrier concentration. Thus, the small effective mass will result in large μ and σ, thereby a high power factor.

The carrier relaxation time can be accurately calculated from the EPI matrix elements. According to Eq. (1), the carrier relaxation time and EPI matrix elements are related by the electron self-energy $\mathrm{Im}(\Sigma)$. The projections of $\mathrm{Im}(\Sigma)$ on the band structure and the energy-dependent carrier relaxation time are displayed in Figs. 3(a) and 3(c), respectively. States with small $\mathrm{Im}(\Sigma)$ appear around the VBM and CBM because electrons and holes near the band edges are less scattered as a result of the limited phase space.[7,47] Moreover, a strong energy dependence can be witnessed from the energy-dependent carrier relaxation time as shown in Fig. 3(c). The carrier relaxation time decreases uniformly with temperature increasing. The relaxation time at 300 K is higher than that at 600 K. This can be easily understood, since more and more phonons are populated with the increase of temperature, which leads the electron–phonon scattering to strengthen.[48]

Figure 4 shows the curves of electronic transport and TE parameters *versus* carrier concentrations at 300 K for n-type and p-type dopings under the SOC+SERTA. Figures 4(a) and 4(b) display the large S values for n-type and p-type doped monolayer square-Au_2S. For instance, the absolute value of S for n-type (p-type) doping at the optimal carrier concentration (corresponding to the maximum ZT) is 265 μV/K (214 μV/K). Both of them are in the range of 200 μV/K–300 μV/K, which is an indicator of good TE material.[1,49] Figures 4(c) and 4(d) show that the σ for n-type doping is superior to that for p-type

doping. Notably, the absolute value of S is inversely proportional to carrier concentration, whereas the σ follows the opposite trend, suggesting that there is a trade-off between them, leading to a maximum PF at a certain carrier concentration.

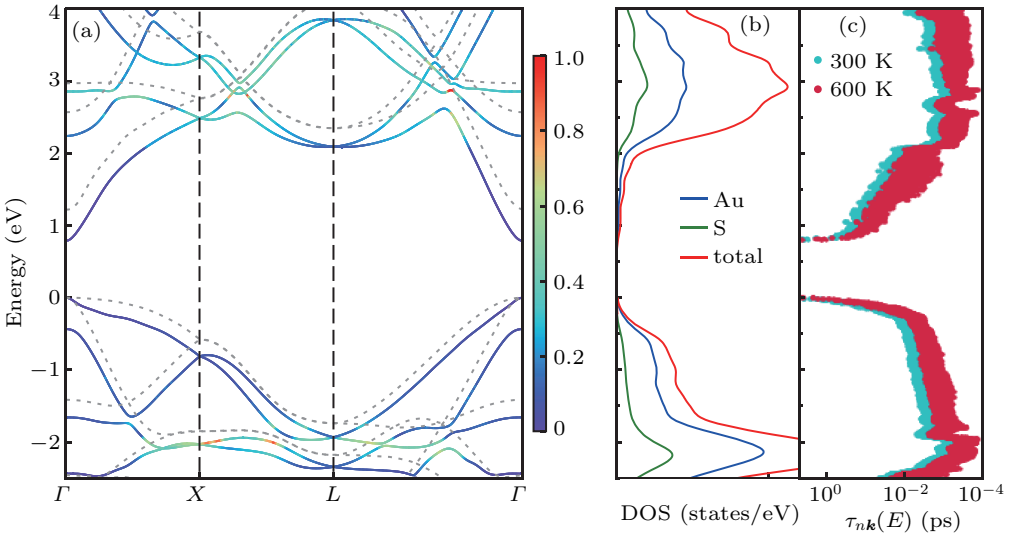


Fig. 3. (a) Electronic band structure calculated by HSE06 functional with (solid line) and without considering the SOC effect (gray dotted line), (b) projected density of states with considering SOC effect, and (c) energy-dependent carrier relaxation time $\tau_{n\boldsymbol{k}}(E)$. Band structure with SOC effect is color-coded according to Im(Σ) at 300 K, which is scaled by color bar with units of eV.

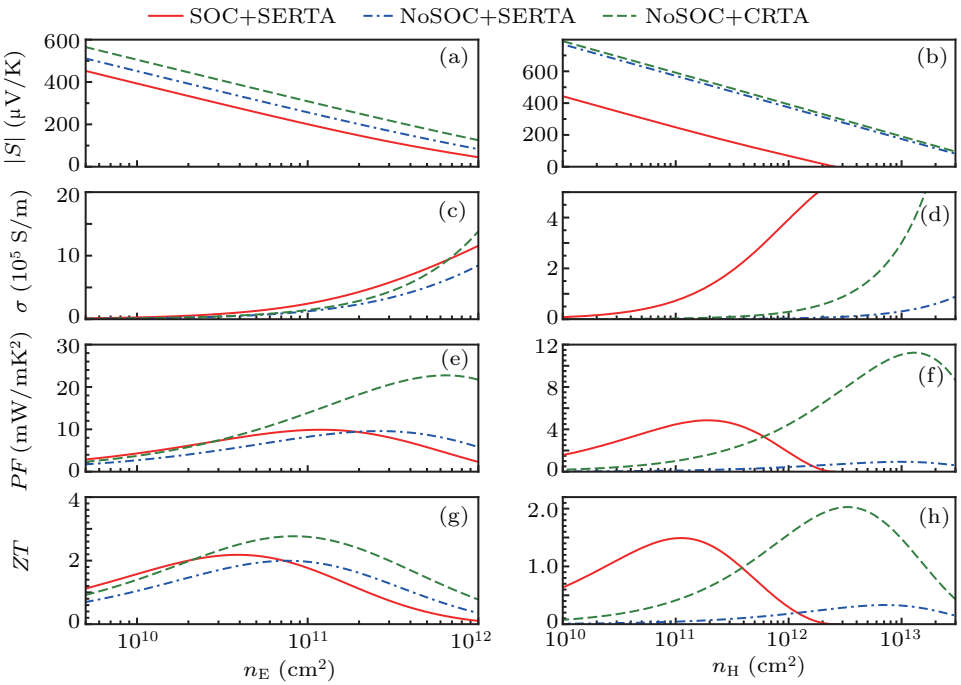


Fig. 4. Curves of electronic transport and TE coefficients *versus* carrier concentration of n-type (left panels) and p-type (right panels) doped monolayer square-Au_2S at 300 K: ((a), (b)) absolute value of Seebeck coefficient S, ((c), (d)) electrical conductivity σ, ((e), (f)) power factor PF, and ((g),(h)) figure of merit ZT.

The calculated PF values in Figs. 4(e) and 4(f) shows that the maximum PF of n-type doping is twice that of p-type doping mainly due to the higher σ for n-type doping. The n-type (p-type) doped monolayer square-Au_2S has an exceptional $PF = 9.90(4.85)$ mW/mK^2 at 300 K, which is higher than that of monolayers δ-Cu_2S and Bi_2O_2Se. The calculated κ_e for n-type (p-type) doping at optimal concentration is 0.38 (0.20) W/mK, which is lower than κ_l. Moreover, the κ_e for n-type (p-type) doping contributes only 34% (21%) to the total κ (see the supplementary material, Fig. S5). Owing to the high PF and quite low κ, the n-type (p-type) ZT of 2.2 (1.5) can be achieved at the optimal hole concentration $n_E \approx 4.0 \times 10^{10}$ cm^{-2} ($n_H \approx 1.1 \times 10^{11}$ cm^{-2}) and $T = 300$ K as shown in Figs. 4(g) and 4(h).

Figure 5 displays the contour map of ZT *versus* temperature and doping concentration under SOC+SERTA. It is found that the maximum ZT and the optimal carrier concentration both increase with temperature increasing. The maximum n-type (p-type) ZT exceeds 3.7 (2.4) at $n_E \approx 8.5 \times 10^{10}$ cm^{-2} ($n_H \approx 4.0 \times 10^{11}$ cm^{-2}) and 600 K. The maximum n-type

$ZT = 3.8$ is higher than that of typical bulk TE material: SnSe (2.6).[50] and 2D monolayers: δ-Cu_2S (1.33),[14] Tl_2O (3.35),[20] and Bi_2O_2Se (3.35).[6]

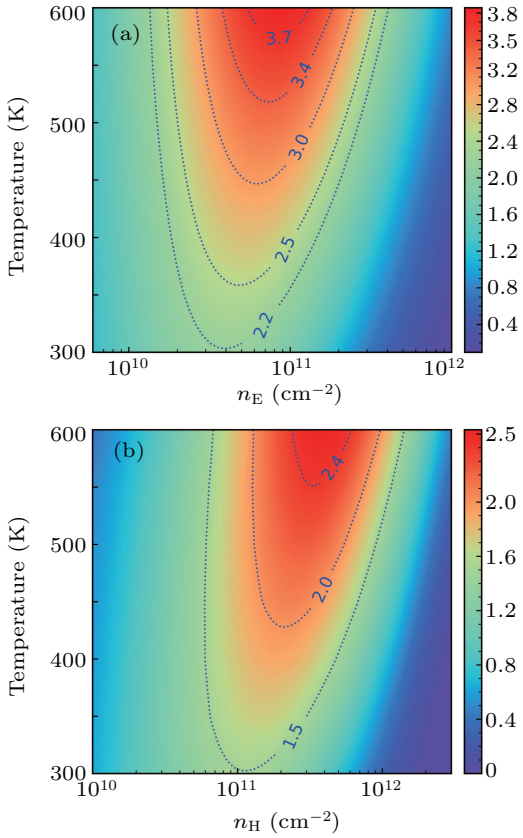


Fig. 5. Contour map of ZT as a function of temperature and carrier concentration of (a) n-type and (b) p-type doped monolayer square-Au_2S.

3.4. Effects of SOC and EPIs on TE properties

The SOC effect and EPIs may play a vital role in determining the electronic properties of materials.[25,30,51,52] The influence of the SOC effect can be revealed by comparing the results from SOC+SERTA and NoSOC+SERTA calculations as shown in Fig. 4. With the consideration of SOC, for p-type doping, S decreases whereas σ increases significantly, which can be understood through the above analyses of band structures. Since the increase of σ is dominant, the maximum PF and ZT with SOC are ~ 4 times and ~ 3.5 times larger than the results without SOC, respectively. Moreover, the optimum hole concentration decreases by nearly two orders of magnitude with SOC strengthening. On the other hand, the band edges around CBM are less affected by the SOC effect as shown in Fig. 3(a). Therefore, for S and σ of n-type doping, the difference between the results with and without the SOC effect is much smaller than the counterparts in the case of p-type doping. Moreover, the maximum values of n-type PF and ZT with and without the SOC effect are close to each other (see the left panel of Fig. 4).

To reveal the influence of EPIs on the electronic transport properties, we compare the results from SERTA and CRTA calculations in Fig. 4. For n-type and p-type dopings, the S from SERTA reasonably accords with that from CRTA, which indicates the low correlation between S and carrier relaxation time. The discrepancy between the CRTA and SERTA results is apparent for σ, κ_e, and the maximum values of PF and ZT, which are shown in Fig. 4 and Fig. S5. The maximum values of PF (ZT) from SERTA are $\sim 56\%$ (28%) and $\sim 90\%$ (84%) lower than those from CRTA for n-type and p-type dopings, respectively. Therefore, the strong energy dependence of $\tau_{nk}(E)$ plays an essential role in determining the overall electronic transport and TE performance. The completely different treatment of carrier relaxation time is responsible for the discrepancy. In the CRTA calculations, the carrier relaxation time is regarded as a constant. It is calculated by the deformation potential theory, which only considers the electron–acoustic phonon scattering. However, for monolayer square-Au_2S, the optical phonon scattering is comparable to that from the acoustic phonon branches (see Fig. S6 in the supplementary material). The SERTA adopts the energy-resolved carrier relaxation time deduced from the EPI matrix elements which take into account all electron–phonon scattering processes. To date, the electronic transport and TE properties of several materials, including Li,[53] Si,[29,30] GaAs,[29] SnSe,[52] Mg_3Sb_2,[24] CoSi,[51] *etc*. have been investigated by the parameter-free algorithm and the calculation results accord well with the experimental data. Therefore, the electronic transport and TE properties of monolayer square-Au_2S obtained by the SERTA are believed to be more predictive than by the CRTA, although the corresponding experimental data are not available at present. In addition, although the maximum values of PF and ZT from the SERTA seriously deviate from those from the CRTA, the optimum carrier concentrations predicted by the two methods are relatively close to each other.

4. Conclusions

In summary, thermal, electronic transport, and thermoelectric properties of monolayer square-Au_2S are systematically investigated via a parameter-free *ab initio* Boltzmann transport algorithm. Owing to the low group velocity and strong anharmonic phonon scattering, the monolayer square-Au_2S possesses an ultralow lattice thermal conductivity κ_l of 0.72 W/mK at 300 K. The square-Au_2S monolayer has extraordinarily high Seebeck coefficient and electrical conductivity. Consequently, the maximum power factor of the n-type (p-type) square-Au_2S monolayer can be as large as 9.90 (4.85) mW/mK^2 at 300 K. Benefiting from the ultralow κ_l and the high power factor, a high room-temperature figure of merit ZT of 2.2 (1.5) can be achieved for n-type (p-type) doping, and it increases up to an ultrahigh value of 3.8 (2.5) at 600 K. In addition, when EPIs are considered, the ZT values are significantly reduced by 28% (84%) for n-type (p-type) doping. Af-

ter introducing the SOC effect, the p-type *ZT* is substantially increased by 3.5 times but the n-type one is almost unaffected. Our analyses strongly suggest that the 2D square-Au_2S monolayer could be a potential candidate for future-generation TE applications.

Acknowledgment

The calculations were carried out on TianHe-2 at the LvLiang Cloud Computing Center in China.

References

[1] Zhou Z Z, Liu H J, Fan D D, Cao G H and Sheng C Y 2018 *ACS Appl. Mater. Interfaces* **10** 37031
[2] Wu Y Y, Zhu X L, Yang H Y, Wang Z G, Li Y H and Wang B T 2020 *Chin. Phys. B* **29** 087202
[3] Lan Y S, Chen X R, Hu C E, Cheng Y and Chen Q F 2019 *J. Mater. Chem. A* **7** 11134
[4] Du B S, Jian J K, Liu H T, Liu J and Qiu L 2018 *Chin. Phys. B* **27** 048102
[5] Hong M, Chen Z G and Zou J 2018 *Chin. Phys. B* **27** 048403
[6] Yu J and Sun Q 2018 *Appl. Phys. Lett.* **112** 053901
[7] He J, Xia Y, Naghavi S S, Ozolins V and Wolverton C 2019 *Nat. Commun.* **10** 719
[8] Guo S D 2016 *J. Mater. Chem. C* **4** 9366
[9] He J, Zhao L D, Zheng J C, Doak J W, Wu H, Wang H Q, Lee Y, Wolverton C, Kanatzidis M G and Dravid V P 2013 *J. Am. Chem. Soc.* **135** 4624
[10] Soni A, Shen Y, Yin M, Zhao Y, Yu L, Hu X, Dong Z, Khor K A, Dresselhaus M S and Xiong Q 2012 *Nano Lett.* **12** 4305
[11] Hicks L D and Dresselhaus M S 1993 *Phys. Rev. B* **47** 12727
[12] Zhu X L, Liu P F, Xie G and Wang B T 2019 *Phys. Chem. Chem. Phys.* **21** 10931
[13] Huang H H, Xing G, Fan X, Singh D J and Zheng W T 2019 *J. Mater. Chem. C* **7** 5094
[14] Yu J, Li T, Nie G, Zhang B P and Sun Q 2019 *Nanoscale* **11** 10306
[15] Shen S, Liang Y, Ma Y, Huang B, Wei W and Dai Y 2018 *Phys. Chem. Chem. Phys.* **20** 14778
[16] Ma Y, Kuc A and Heine T 2017 *J. Am. Chem. Soc.* **139** 11694
[17] Sharma S, Shafique A and Schwingenschlögl U 2020 *ACS Appl. Energy Mater.* **3** 10147
[18] Chen X, Wang D, Liu X, Li L and Sanyal B 2020 *J. Phys. Chem. Lett.* **11** 2925
[19] Wu Q, Xu W W, Lin D, Wang J and Zeng X C 2019 *J. Phys. Chem. Lett.* **10** 3773
[20] Wang C, Wei S and Gao G 2019 *ACS Appl. Nano Mater.* **2** 4061
[21] Yang L M, Bačić V, Popov I A, Boldyrev A I, Heine T, Frauenheim T and Ganz E 2015 *J. Am. Chem. Soc.* **137** 2757
[22] Bardeen J and Shockley W 1950 *Phys. Rev.* **80** 72
[23] Bruzzone S and Fiori G 2011 *Appl. Phys. Lett.* **99** 222108
[24] Meng F, Sun S, Ma J, Chronister C, He J and Li W 2020 *Mater. Today Phys.* **13** 100217
[25] Ma J, Meng F, He J, Jia Y and Li W 2020 *ACS Appl. Mater. Interfaces* **12** 43901
[26] Cutler M and Mott N F 1969 *Phys. Rev.* **181** 1336
[27] Madsen G K H, Carrete J and Verstraete M J 2018 *Comput. Phys. Commun.* **231** 140
[28] Ziman J M 1960 *Electrons and Phonons: The Theory of Transport Phenomena in Solids* (Oxford: Clarendon Press)
[29] Ma J, Nissimagoudar A S and Li W 2018 *Phys. Rev. B* **97** 045201
[30] Poncé S, Margine E R and Giustino F 2018 *Phys. Rev. B* **97** 121201
[31] Giannozzi P, Baroni S, Bonini N, Calandra M, Car R, Cavazzoni C, Ceresoli D, Chiarotti G L, Cococcioni M, Dabo I, Dal Corso A, de Gironcoli S, Fabris S, Fratesi G, Gebauer R, Gerstmann U, Gougoussis C, Kokalj A, Lazzeri M, Martin-Samos L, Marzari N, Mauri F, Mazzarello R, Paolini S, Pasquarello A, Paulatto L, Sbraccia C, Scandolo S, Sclauzero G, Seitsonen A P, Smogunov A, Umari P and Wentzcovitch R M 2009 *J. Phys.: Condens. Matter* **21** 395502
[32] Perdew J P, Burke K and Ernzerhof M 1996 *Phys. Rev. Lett.* **77** 3865
[33] Hamann D R 2013 *Phys. Rev. B* **88** 085117
[34] Grimme S, Antony J, Ehrlich S and Krieg H 2010 *J. Chem. Phys.* **132** 154104
[35] Li W, Carrete J, A. Katcho N and Mingo N 2014 *Comput. Phys. Commun.* **185** 1747
[36] Bondi A 1964 *J. Phys. Chem.* **68** 441
[37] Gao Z, Tao F and Ren J 2018 *Nanoscale* **10** 12997
[38] Zhu X L, Liu P F, Zhang J, Zhang P, Zhou W X, Xie G and Wang B T 2019 *Nanoscale* **11** 19923
[39] Poncé S, Margine E R, Verdi C and Giustino F 2016 *Comput. Phys. Commun.* **209** 116
[40] Noffsinger J, Giustino F, Malone B D, Park C H, Louie S G and Cohen M L 2010 *Comput. Phys. Commun.* **181** 2140
[41] Sun Y, Shuai Z and Wang D 2019 *J. Phys. Chem. C* **123** 12001
[42] Zhang J, Liu H J, Cheng L, Wei J, Shi J, Tang X F and Uher C 2014 *J. Appl. Phys.* **116** 023706
[43] Jin Z, Liao Q, Fang H, Liu Z, Liu W, Ding Z, Luo T and Yang N 2015 *Sci. Rep.* **5** 18342
[44] Zhou Z Z, Liu H J, Fan D D and Cao G H 2019 *J. Phys.: Condens. Matter* **31** 385701
[45] Fan D D, Liu H J, Cheng L, Liang J H and Jiang P H 2018 *J. Mater. Chem. A* **6** 12125
[46] Huang Y, Zhou J, Wang G and Sun Z 2019 *J. Am. Chem. Soc.* **141** 8503
[47] Zhao Y, Dai Z, Lian C, Zeng S, Li G, Ni J and Meng S 2017 *Phys. Rev. Mater.* **1** 065401
[48] Giustino F, Cohen M L and Louie S G 2007 *Phys. Rev. B* **76** 165108
[49] Hung N T, Nugraha A R T and Saito R 2017 *Appl. Phys. Lett.* **111** 092107
[50] Zhao L D, Lo S H, Zhang Y, Sun H, Tan G, Uher C, Wolverton C, Dravid V P and Kanatzidis M G 2014 *Nature* **508** 373
[51] Xia Y, Park J, Zhou F and Ozoliņš V 2019 *Phys. Rev. Appl.* **11** 024017
[52] Ma J, Chen Y and Li W 2018 *Phys. Rev. B* **97** 205207
[53] Xu B and Verstraete M J 2014 *Phys. Rev. Lett.* **112** 196603
[54] Ouyang T, Jiang E, Tang C, Li J, He C and Zhong J 2018 *J. Mater. Chem. A* **6** 21532